


Non-Abelian topological superconductivity in maximally twisted double-layer spin-triplet valley-singlet superconductors

Benjamin T. Zhou ¹, Shannon Egan¹, Dhruv Kush¹ & Marcel Franz ¹

Recent studies point to an exotic spin-triplet valley-singlet (STVS) superconducting phase in certain two-valley electron liquids, including rhombohedral trilayer graphene, Bernal bilayer graphene and ZrNCl, which nevertheless admits only trivial topology. Here, we predict that upon twisting two layers of STVS superconductors, a chiral $f \pm if'$ -wave superconducting phase emerges near the 'maximal' twist angle of 30° where the system becomes an extrinsic quasi-crystal with 12-fold tiling. The resulting composite hosts an odd number of chiral Majorana edge modes and a single non-Abelian Majorana zero mode (MZM) in the vortex core. Through detailed symmetry analysis and microscopic modelling, we demonstrate that the non-Abelian topological superconductivity (TSC) forms robustly near the maximal twist when the isolated Fermi pockets coalesce into a single connected Fermi surface in the moiré Brillouin zone. Our results establish the large-twist-angle engineering, with distinct underlying moiré physics from magic-angle graphene, as a viable route toward non-Abelian TSC.

¹Department of Physics and Astronomy & Stewart Blusson Quantum Matter Institute, University of British Columbia, Vancouver, BC V6T 1Z4, Canada.
email: benjamin.zhou@ubc.ca; franz@phas.ubc.ca

Being of fundamental interest and potential use for topological qubits, the search for topological superconductors hosting excitations with non-Abelian exchange statistics has been one of the central topics in condensed matter physics over the past two decades^{1–5}. The simplest such particles—Majorana zero modes (MZMs) – were originally proposed as vortex core states in chiral p -wave superconductors^{6–8}, but the lack of intrinsic p -wave superconductivity in nature has motivated worldwide efforts to engineer synthetic platforms that emulate this behavior using more conventional ingredients^{9–17}. Whether such effective p -wave superconductors and MZMs have been realized in recent experiments is still under debate^{18–20}. The quest for an intrinsic topological superconductor with non-Abelian excitations, on the other hand, remains an ongoing grand challenge to the condensed matter community.

Motivated by recent developments in twisted van der Waals materials^{21–29}, a new route toward topological superconductivity (TSC) has been proposed recently which takes two monolayers of high- T_c cuprate superconductor with nodal $d_{x^2-y^2}$ pairing symmetry, such as $\text{Bi}_2\text{Sr}_2\text{CaCu}_2\text{O}_{8+\delta}$, stacked with a relative angular twist θ ^{30,31}. At $\theta \simeq 45^\circ$, the bilayer is predicted to enter a fully-gapped, topological chiral $d \pm id'$ phase with spontaneously broken time-reversal symmetry \mathcal{T} , which has been tentatively identified in a recent experimental study³². Despite its promise for realizing high- T_c TSC, a chiral $d \pm id'$ superconductor cannot host truly non-Abelian excitations due to its spin-singlet pairing nature, which is always associated with an even number of MZMs that combine to form usual Abelian fermions. Generalizing the scheme to spin-triplet superconductors with nodal p -wave or f -wave order parameters one can create chiral SC phases with an odd number of MZMs in principle³³, while once again facing the scarcity of nodal p -wave and f -wave superconductors in nature.

Recent progress in superconducting two-dimensional materials, however, has uncovered a growing amount of evidence for f -wave spin-triplet superconductivity, albeit in the guise of a fully gapped phase: in a recent experiment, rhombohedral trilayer graphene (RTG) was found to superconduct in two different gate-tuned regions, where the peculiar SC2 superconducting phase was borne out of a spin-polarized, valley-unpolarized normal metal³⁴. Such an unusual normal-state fermiology strongly hints at its spin-triplet pairing nature, which is further supported by the observation of an in-plane critical field that far exceeds the Pauli paramagnetic limit. Similar results have also been reported in Bernal bilayer graphene (BBG)³⁵, and both experimental observations were interpreted theoretically as a signature of spin-triplet f -wave pairing^{36,37}. More recently, Crépel and Fu proposed that a ‘three-particle’ mechanism involving virtual excitons generically gives rise to spin-triplet f -wave pairing in a two-valley electron liquid formed in doped insulators such as ZrNCl ³⁸, which provides a plausible explanation for the puzzling doping dependence of the gap structure revealed by early specific heat measurements on Li-doped ZrNCl ³⁹.

In the scenarios described above, the parent normal-state Fermi surface (FS) consists of disconnected pockets enclosing the $+K$ and $-K$ corners of the hexagonal Brillouin zone (BZ), as illustrated in Fig. 1a. Upon pairing electrons of the same spin and from opposite valleys, fermion exchange statistics require the order parameter to be odd under exchange of the valleys, which entails a spin-triplet valley-singlet (STVS) pairing. As shown schematically in Fig. 1a, such an STVS superconductor has exactly the $f_{x(x^2-3y^2)}$ -wave symmetry, while the excitation spectrum exhibits a full superconducting gap because the nodes of the f -wave gap function (located along $\Gamma - M$ lines) never intersect the disconnected FS. The gapped phase respects a spinless time-reversal symmetry \mathcal{T}' and particle-hole symmetry \mathcal{P} (such that

$\mathcal{T}'^2 = \mathcal{P}^2 = +1$) and thus belongs to symmetry class BDI in Altland–Zirnbauer classification⁴⁰. In two space dimensions, BDI class admits only trivial topology implying that the STVS superconductor is topologically trivial.

Here, we show that stacking two layers of STVS superconductor with an angular twist θ close to 30° creates an intrinsic chiral $f \pm if'$ -wave topological superconductor as the disconnected FSs around K -valleys in each isolated layer coalesce into a connected FS in the twisted double-layer under moiré band folding at large-angle twist. This \mathcal{T}' -broken phase belongs to symmetry class D and admits nontrivial topology indicated by integer-valued Chern number C . Our results, based on symmetry analysis and detailed microscopic modeling, show that for $\theta \simeq 30^\circ \pm 0.3^\circ$, the chiral $f \pm if'$ phase occurs robustly throughout a wide range of electron density and, at exactly 30° twist where the system has a high 12-fold quasi-crystalline symmetry, extends up to the native critical temperature of the double-layer superconductor. Within the chemical potential range where the disconnected K -pockets from the two layers merge into a single FS, we find $C = \pm 3$, indicating non-Abelian topology manifested through an odd number of chiral Majorana modes on its edge and a single MZM in the core of its superconducting vortex (Fig. 1b). As θ deviates from 30° , the chiral topological phase evolves into a nodal topological $f_{x(x^2-3y^2)}$ -wave superconductor, in which nodes of opposite chiralities in the bulk are connected by non-dispersive MZMs on one of the system edges, analogous to flat bands present on zigzag edges of monolayer graphene^{41,42}. Our results establish the large-twist-angle moiré physics, which is absent in twisted cuprates and also fundamentally different from the small-angle moiré physics in magic-angle twisted graphene (see the comparison in Supplementary Note 1), as a viable route toward non-Abelian TSC.

Results

Normal-state fermiology. For the sake of concreteness and simplicity, we describe the normal state of a monolayer STVS superconductor by a triangular lattice tight-binding model with nearest-neighbor electron hopping $-t$ (Fig. 2a). Such Hamiltonians are widely used to model systems with hexagonal symmetry whose FS consist of disconnected segments around K -points^{38,43} shown in Fig. 2b. Motivated by the phenomenology observed in RTG and BBG systems^{34,35} and by theoretical ideas introduced in ref. 38, we focus here on equal-spin pairing between electrons belonging to opposite valleys and drop the spin index in our discussions. Moreover, we consider hole doping near K -points by setting $t > 0$ with band maxima located at $\pm K$ given by $E_{\max} = 3t$ in each isolated layer (the case of electron doping can be covered by setting $t < 0$ with $E_{\min} = 3t$). Throughout this work, we follow the convention that \mathbf{k} , \mathbf{R} , \mathbf{G} respectively denote the Bloch momenta, real-space lattice vectors, and reciprocal lattice vectors in layer 1, while $\tilde{\mathbf{k}}$, $\tilde{\mathbf{R}}$, $\tilde{\mathbf{G}}$ stand for their counterparts in layer 2. Given lattice vectors $\mathbf{R}^{(0)}$ and reciprocal lattice vectors $\mathbf{G}^{(0)}$ in an unrotated triangular lattice (open circles in Fig. 2a), we have $\mathbf{R} = R_z(\theta/2)\mathbf{R}^{(0)}$, $\tilde{\mathbf{R}} = R_z(-\theta/2)\tilde{\mathbf{R}}^{(0)}$ and $\mathbf{G} = R_z(\theta/2)\mathbf{G}^{(0)}$, $\tilde{\mathbf{G}} = R_z(-\theta/2)\tilde{\mathbf{G}}^{(0)}$, with $R_z(\theta)$ being the rotation of θ about the z -axis.

Upon an angular twist θ , the normal-state Hamiltonians of the two decoupled layers are given by

$$\begin{aligned} \mathcal{H}_0^{(1)} &= \sum_{\mathbf{k}} \xi_1(\mathbf{k}) c_1^\dagger(\mathbf{k}) c_1(\mathbf{k}), \\ \mathcal{H}_0^{(2)} &= \sum_{\tilde{\mathbf{k}}} \xi_2(\tilde{\mathbf{k}}) c_2^\dagger(\tilde{\mathbf{k}}) c_2(\tilde{\mathbf{k}}), \end{aligned} \quad (1)$$

where $\xi_1(\mathbf{k}) = -2t \sum_{j=1,3,5} \cos(\mathbf{k} \cdot \mathbf{R}_j) - \mu$ is the kinetic energy term in layer 1, and $\xi_2(\tilde{\mathbf{k}}) = -2t \sum_{j=1,3,5} \cos(\tilde{\mathbf{k}} \cdot \tilde{\mathbf{R}}_j) - \mu$ in layer 2,

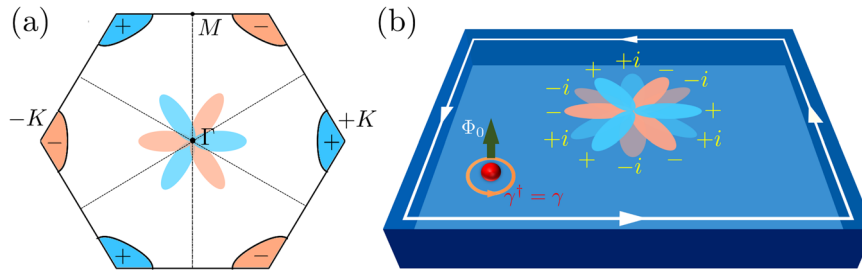


Fig. 1 Emergence of chiral $f \pm if'$ -wave superconductivity in maximally twisted double-layer spin-triplet valley-singlet (STVS) superconductors.

a Structure of the $f_{x(x^2-3y^2)}$ -wave order parameter in the spin-triplet valley-singlet (STVS) superconductor. Gap nodes along Γ - M (dashed lines) are avoided by disconnected Fermi pockets around $\pm K$ resulting in a fully-gapped phase. **b** Schematic of a chiral $f \pm if'$ phase formed by twisting two layers of STVS superconductors at $\theta \approx 30^\circ$. Chiral Majorana edge modes (white arrows) emerge on the edge and a single Majorana zero mode denoted by $\hat{\gamma}$ (red dot) forms at the vortex core threaded by a unit flux Φ_0 .

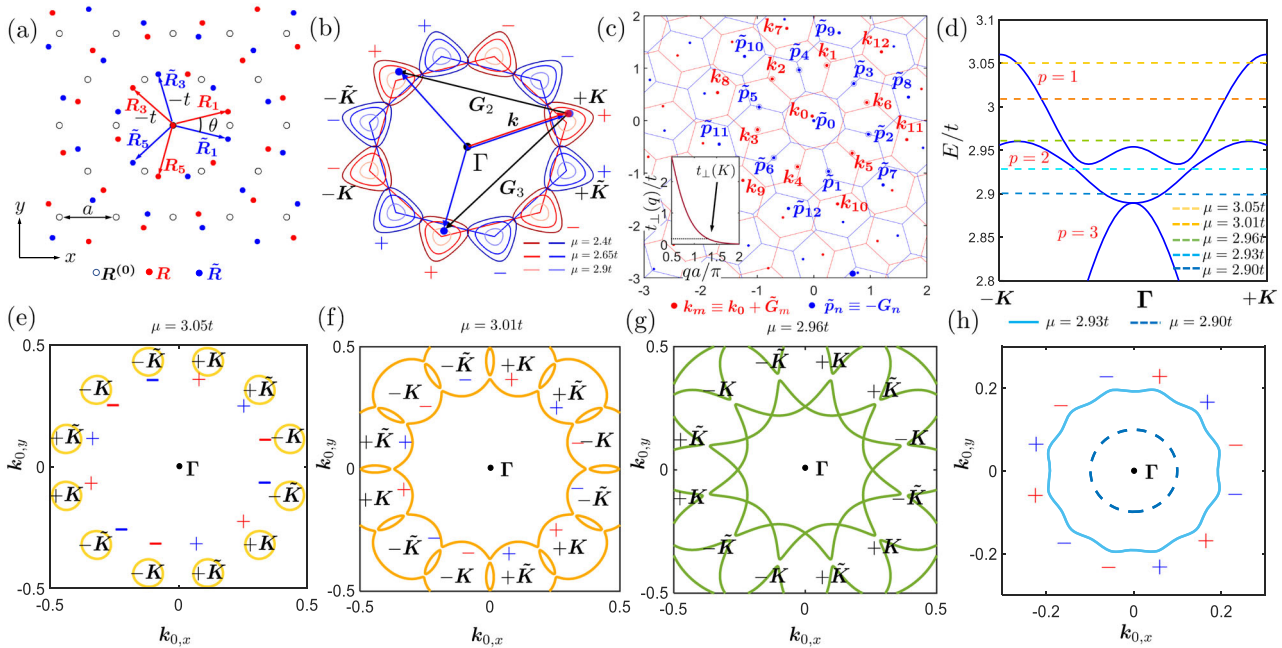


Fig. 2 Modeling normal-state fermiology in double-layer two-valley electron liquids with 30° twist. **a** Real-space triangular lattices for two layers of spin-triplet valley-singlet (STVS) superconductors stacked with angular twist θ . Dots in red (blue) denote lattice sites \mathbf{R} ($\bar{\mathbf{R}}$) in layer 1 (2) with lattice constant $a = 2.46 \text{ \AA}$. Hopping parameter $t = 1 \text{ eV}$ in all figures. **b** Fermi surface (FS) contours around $\pm K$ points of two decoupled layers at $\theta = 30^\circ$ for chemical potential $2.4t < \mu < 3t$. $\mathbf{G}_2, \mathbf{G}_3$ denote reciprocal lattice vectors in layer 1. **c** Dual-momentum space lattice points \mathbf{k}_m (red dots) and $\bar{\mathbf{p}}_n$ (blue dots) for a fixed momentum \mathbf{k}_0 in units of $2\pi/a$ (see subsection “Dual momentum-space tight-binding model” in Methods). Red (blue) hexagons denote Wigner-Seitz cells in reciprocal lattice of layer 1 (2). Note that the original location of each \mathbf{k}_m in the first Brillouin zone is exactly the location measured from the center of the red hexagon that contains it. Bloch momenta near $\pm K$ and $\pm \bar{K}$ in **(b)** are covered by $m, n = 1, 2, \dots, 6$ (encircled dots) as \mathbf{k}_0 varies in momentum-space. Inset: Fourier transform $t_\perp(\mathbf{q})$ of inter-layer coupling, $t_\perp(K)$ extrapolated at $Ka/\pi = 4/3$. **d** Band structure of $\mathcal{H}_{0,\text{eff}}$ with topmost bands indexed by $p = 1, 2, 3$. Dashed lines indicate chemical potentials of FS contours shown in **(e-h)**. Units of $k_{0,x}, k_{0,y}$ axes are in \AA^{-1} . Red (blue) \pm symbols indicate signs of pairing in layer 1 (2).

μ is the chemical potential. For $\mu \in (2t, 3t)$, the triangular lattice model produces disconnected Fermi pockets around K and $-K$ points shown in Fig. 2b.

Studies of twisted 2D materials have established that the interlayer coupling within a twisted bilayer structure has the general form^{21,24,44–46}

$$\begin{aligned} \mathcal{H}_T &= \sum_{\mathbf{k}, \tilde{\mathbf{k}}} \left[c_1^\dagger(\mathbf{k}) T(\mathbf{k}, \tilde{\mathbf{k}}) c_2(\tilde{\mathbf{k}}) + \text{h.c.} \right] \\ T(\mathbf{k}, \tilde{\mathbf{k}}) &= - \sum_{\mathbf{G}, \tilde{\mathbf{G}}} t_\perp(\mathbf{k} + \mathbf{G}) \delta_{\mathbf{k} + \mathbf{G}, \tilde{\mathbf{k}} + \tilde{\mathbf{G}}}, \end{aligned} \quad (2)$$

where $t_\perp(\mathbf{q})$ is the Fourier transform of the inter-layer coupling $t_\perp(\mathbf{r})$ as a function of spatial separation \mathbf{r} between two atomic positions in different layers. It is worth noting that $t_\perp(\mathbf{q})$ decays

rapidly as a function of $|\mathbf{q}|$ in general and becomes negligibly small on the scale of $q \approx 2\pi/a$ where a denotes the monolayer lattice constant. To be concrete, we model $t_\perp(\mathbf{r})$ by an empirical exponential formula describing σ -bonds formed by p_z -orbitals from the two layers (see Supplementary Note 2) and extrapolate an effective interlayer coupling strength of $t_\perp(K) \approx 0.15t$ for states near K -points (inset of Fig. 2c).

In twisted cuprates, superconductivity is borne out of large Fermi surfaces and Dirac nodes of the d -wave order parameter are located well inside the Brillouin zone of each layer. The leading-order inter-layer coupling according to Eq. (2) is simply the momentum-preserving term with $\mathbf{k} = \tilde{\mathbf{k}}$ and $\mathbf{G} = \tilde{\mathbf{G}} = 0$. This allows treating the inter-layer coupling as a constant in the continuum model in which moiré effects are inessential³⁰. In

contrast, superconductivity in an STVS superconductor emerges from two disconnected pockets surrounding the $+K$ and $-K$ points, and, as indicated in Fig. 2b, the leading-order inter-layer terms for a Bloch state with momentum $\mathbf{k} \simeq \pm \mathbf{K}$ in layer 1 include three different processes connecting it to states in layer 2 at $\tilde{\mathbf{k}} = (\mathbf{k}, \mathbf{k} + \mathbf{G}_2, \mathbf{k} + \mathbf{G}_3)$. The momentum transfer processes above are central ingredients in the celebrated Bistritzer-MacDonald (BM) model of small-angle twisted bilayer graphene²¹ and its variants for other twisted materials with two K -valleys^{24,46}, where the two valleys are modeled separately by valley-dependent low-energy effective Hamiltonians. However, the BM-type continuum model designed for the small twist-angle limit will fail to describe the maximally twisted double-layer STVS superconductor. This is because for $\theta \simeq 30^\circ$, the three different momenta $\tilde{\mathbf{k}}$ in layer 2 are located midway between the $+\tilde{K}$ and $-\tilde{K}$ points (Fig. 2b), where the low-energy Hamiltonian defined for a single valley is no longer valid.

To overcome this difficulty we develop our own method based on the dual momentum-space tight-binding (DMSTB) model (see Methods section) introduced in a recent theoretical study of quasi-crystalline electronic bands in 30° twisted bilayer graphene⁴⁵. This approach was motivated and validated by experimental work^{47,48}. The authors showed that stacking two identical layers with honeycomb lattice geometries at an exact 30° twist results in an extrinsic quasi-crystal with 12-fold tiling but no exact crystalline symmetries. They further argued that owing to the limited number of leading-order inter-layer processes discussed above, it is possible to construct an effective momentum-space Hamiltonian of a relatively small size. We adapted this method to our triangular lattice geometry to construct an effective Hamiltonian $\mathcal{H}_{0,\text{eff}}$ based on the dual momentum-space lattice sites $\mathbf{k}_{m=0,\dots,12}$ and $\tilde{\mathbf{p}}_{n=0,\dots,12}$ (see subsection “Dual momentum-space tight-binding model” in Methods and Supplementary Note 3 for details) shown in Fig. 2c and generalized it to arbitrary twist angles close to 30° . Within this description moiré bands due to the large angular twist $\theta \simeq 30^\circ$ can be well defined up to the leading-order approximation, with \mathbf{k}_0 serving as the momentum in the moiré Brillouin zone.

The moiré bands of $\mathcal{H}_{0,\text{eff}}$ at $\theta = 30^\circ$ are solved by exact numerical diagonalization (topmost bands labeled by $p = 1, 2, 3$ shown in Fig. 2d), and the evolution of the Fermi surface upon increasing the doping level is presented in Fig. 2e–h. Due to level repulsion caused by inter-layer coupling, the band maxima at all K -points are shifted to $E_{\text{max}} \simeq 3.06t$. At light hole doping $\mu > 3.01t$, the Fermi surface consists of 12 disconnected pockets stemming from the 12 dual momentum-space sites in Fig. 2c, and resembles the disconnected Fermi surfaces in the decoupled limit (Fig. 2b). It is important to note that due to the moiré band-folding effects introduced by large angle twist, the Fermi surface in the twisted double layer quickly undergoes a Lifshitz transition as doping level increases and becomes connected already at $\mu \simeq 3.01t$ (Fig. 2f), at which point the Fermi pockets in the decoupled limit would still remain well isolated (Fig. 2b).

Upon further doping, the Fermi surface undergoes a second Lifshitz transition at $\mu \simeq 2.96t$ (Fig. 2g) and the system enters a regime with a single connected Fermi surface centered at the Γ point (Fig. 2h). Such FS then remains stable over a wide range of chemical potentials with higher hole doping (Fig. 2d). Crucially, as we show in the next section, at doping levels where a single connected FS exists, the twisted double-layer STVS material at $\theta \simeq 30^\circ$ becomes an intrinsic chiral $f \pm if'$ superconductor with non-Abelian excitations.

Chiral $f \pm if'$ -wave superconductivity at $\theta \simeq 30^\circ$. While microscopic mechanisms leading to STVS superconductivity may vary

across materials such as RTG/BBG^{36,37} and ZrNCl ³⁸, on general grounds the interaction responsible for STVS pairing boils down to an effective attraction between electrons in the spin-triplet f -wave channel. In the momentum-space representation, the interaction within each isolated layer of STVS superconductor has the form

$$\begin{aligned} \mathcal{V}^{(1)} &= -U_0 \sum_{\mathbf{k}, \mathbf{k}'} f_1(\mathbf{k}) f_1(\mathbf{k}') c^\dagger(\mathbf{k}) c^\dagger(-\mathbf{k}) c(-\mathbf{k}') c(\mathbf{k}'), \\ \mathcal{V}^{(2)} &= -U_0 \sum_{\tilde{\mathbf{k}}, \tilde{\mathbf{k}'}} f_2(\tilde{\mathbf{k}}) f_2(\tilde{\mathbf{k}'}) c^\dagger(\tilde{\mathbf{k}}) c^\dagger(-\tilde{\mathbf{k}}) c(-\tilde{\mathbf{k}'}) c(\tilde{\mathbf{k}'}), \end{aligned} \quad (3)$$

where U_0 denotes the interaction strength, and $f_{1,2}$ are the basis functions, $f_1(\mathbf{k}) = \sum_{j=1,3,5} \sin(\mathbf{k} \cdot \mathbf{R}_j)$ and $f_2(\tilde{\mathbf{k}}) = \sum_{j=1,3,5} \sin(\tilde{\mathbf{k}} \cdot \tilde{\mathbf{R}}_j)$, with exact f -wave symmetries shown in Fig. 1a. For isolated layer 1, one can define the self-consistent mean field $\Delta_1 = -U_0 \sum_{\mathbf{k}} f_1(\mathbf{k}') \langle c(-\mathbf{k}') c(\mathbf{k}') \rangle$, and the corresponding gap function $\Delta_1(\mathbf{k}) = \Delta_1 f_1(\mathbf{k})$. Similarly, $\Delta_2(\tilde{\mathbf{k}}) = \Delta_2 f_2(\tilde{\mathbf{k}})$ for isolated layer 2. Note that $\Delta_1(\mathbf{k})$ and $\Delta_2(\tilde{\mathbf{k}})$ are almost constant near $\pm K$ and $\pm \tilde{K}$ but exhibit a valley-dependent sign, as $f_1(\mathbf{k} \simeq \pm \mathbf{K}), f_2(\tilde{\mathbf{k}} \simeq \pm \tilde{\mathbf{K}}) \simeq \mp \frac{3\sqrt{3}}{2}$.

As the disconnected K -pockets in two layers merge into a single connected Fermi surface in the twisted double-layer (Fig. 2h), the piecewise constant gap functions with alternating signs are transformed into continuous functions along the single circular Fermi contour in \mathbf{k}_0 -space. Signs of $\Delta_1(\mathbf{k})$ and $\Delta_2(\tilde{\mathbf{k}})$, indicated by red and blue “ \pm ” symbols in Fig. 2h, are seen to resemble two orthogonal f -wave components superimposed on top of each other. As the Fermi surface gets reconnected in \mathbf{k}_0 -space via inter-layer coupling, it is easy to see that nodes in each of the f -wave components are recovered – if time-reversal remains unbroken and hence the order parameters are real. This happens because the projected pairing on the Fermi surface from each layer must change continuously and a nodal point is mandated whenever a sign change in real order parameter occurs. In analogy with twisted d -wave superconductors³⁰, this suggests that, in order to avoid node formation and thus lower the overall superconducting free energy, the twisted STVS double-layer may develop a spontaneous complex phase difference between the order parameters of the two layers. This realizes the chiral $f \pm if'$ phase.

In the following we support this intuitive picture of the chiral T -broken phase formation with an explicit microscopic calculation. We note that the self-consistency of $\Delta_1(\mathbf{k})$ and $\Delta_2(\tilde{\mathbf{k}})$ in isolated layer 1 and layer 2 implicitly rests upon the translational invariance within each decoupled layer. Upon introducing the inter-layer coupling, this translational symmetry is strongly modified. This forces us to reformulate the superconducting gap equations in terms of wave functions and energy bands derived from the DMSTB model $\mathcal{H}_{0,\text{eff}}$ (see subsection “Mean-field gap equation for twisted double-layer STVS superconductors” of Methods section), so that effects from inter-layer coupling are properly incorporated. In the following, we focus on the topmost three bands indexed by $p = 1, 2, 3$ (inset of Fig. 2d) that are accessible by experimentally relevant doping levels.

In terms of fermionic operators $a_p^\dagger(\mathbf{k}_0)$ which create electrons at \mathbf{k}_0 in band p , the Bogoliubov-de Gennes (BdG) Hamiltonian for the superconducting state in the twisted double-layer

$$\begin{aligned} \mathcal{H}_{\text{BdG}} &= \sum_{p, \mathbf{k}_0} \xi_p(\mathbf{k}_0) a_p^\dagger(\mathbf{k}_0) a_p(\mathbf{k}_0) \\ &+ \sum_{p, \mathbf{k}_0} \left[\Delta_p(\mathbf{k}_0) a_p^\dagger(\mathbf{k}_0) a_p^\dagger(-\mathbf{k}_0) + \text{h.c.} \right], \end{aligned} \quad (4)$$

where $\xi_p(\mathbf{k}_0) = E_p(\mathbf{k}_0) - \mu$ with $E_p(\mathbf{k}_0)$ the kinetic energy of band p , and $\Delta_p(\mathbf{k}_0)$ the pairing in band p : $\Delta_p(\mathbf{k}_0) = \Delta_{1,p} f_{1,p}(\mathbf{k}_0) + \Delta_{2,p} f_{2,p}(\mathbf{k}_0)$, where $f_{i,p}(\mathbf{k}_0)$ are dimensionless basis functions

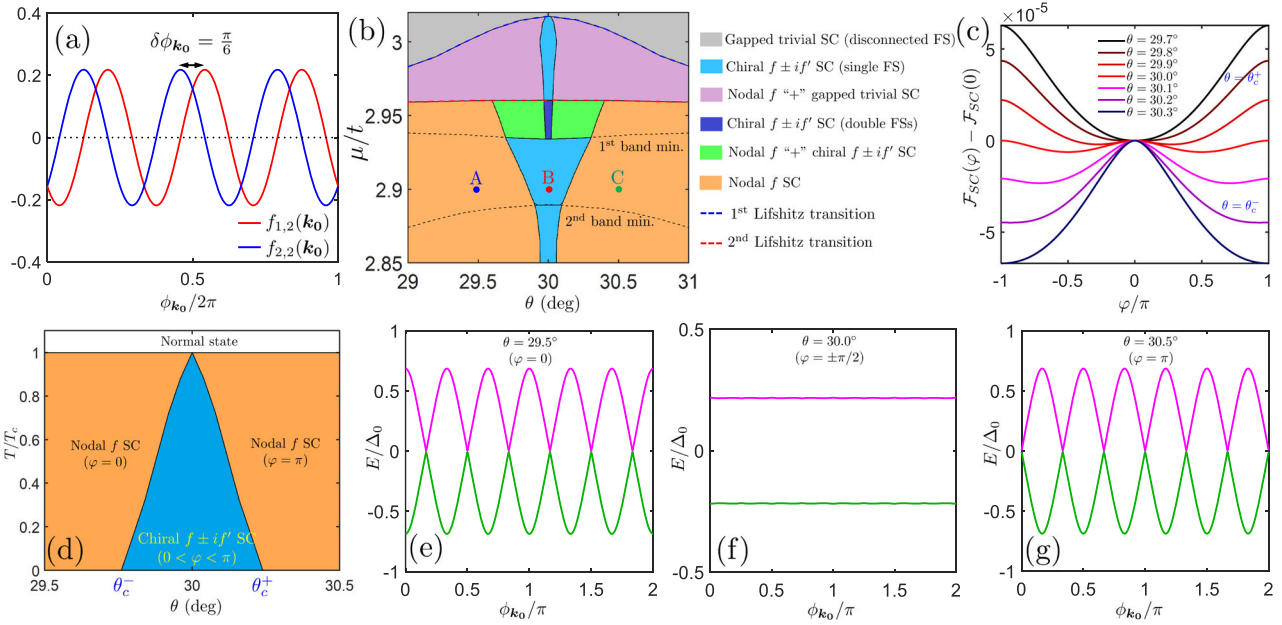


Fig. 3 Chiral $f \pm if'$ superconductivity at 30° twist. **a** Basis functions $f_{1,p}(\mathbf{k}_0)$, $f_{2,p}(\mathbf{k}_0)$ of the projected pair wavefunctions in band $p = 2$ along the circular Fermi surface of twisted-double layer at $\mu = 2.9t$ with momentum radius $|\mathbf{k}_0| \approx 0.11 \text{ \AA}^{-1}$ shown in Fig. 2d. $\phi_{\mathbf{k}_0}$ is the polar angle of \mathbf{k}_0 in the 2D plane. A relative shift of $\delta\phi_{\mathbf{k}_0} = \pi/6$ is found between $f_{1,p}(\mathbf{k}_0)$ and $f_{2,p}(\mathbf{k}_0)$ due to 30° -twist. **b** Phase diagram of a twisted double-layer spin-triplet valley-singlet (STVS) superconductor in the μ - θ plane. A robust chiral $f \pm if'$ phase (regions depicted in blue) is found over the entire chemical potential range for $\theta \approx 30^\circ$. **c** Evolution of phase dependence of the superconducting free energy $\mathcal{F}_{SC}(\varphi)$ as a function of twist angle θ at $\mu = 2.9t$. Unit of y-axis set in eV. **d** Phase diagram in the T - θ plane obtained at $\mu = 2.9t$ and coupling constant $U_0 = 0.013t$, corresponding to critical temperature $T_c \approx 3K$. **e-g** Bulk Bogoliubov excitation gap at **(e)** $\theta = 29.5^\circ$, **(f)** $\theta = 30.0^\circ$, and **(g)** $\theta = 30.5^\circ$, corresponding to dots A, B, and C in **(b)**, respectively. $\Delta_0 = 1 \text{ meV}$ is used here in line with values of μ , U_0 used in **(d)**.

characterizing the projected pairings in the moiré Brillouin zone for layer l and band p . The relations between $f_{l,p}(\mathbf{k}_0)$ and $f_l(\mathbf{k}), f_2(\tilde{\mathbf{k}})$ in Eq. (3) are explicitly given in subsection “Mean-field gap equation for twisted double-layer STVS superconductors” of Methods. Note that mean-fields $\Delta_{1,p}, \Delta_{2,p}$ serve as the superconducting order parameters in moiré band p of layer 1 and layer 2, respectively.

To demonstrate that the projected pairings from layer 1 and 2 form two orthogonal f -wave components at $\theta = 30^\circ$, we plot the dimensionless basis functions $f_{l,p}(\mathbf{k}_0)$ for projected pairing in band $p = 2$ along the circular Fermi surface in the moiré Brillouin zone (Fig. 2d) at $\mu = 2.9t$ in Fig. 3a. Clearly, $f_{1,2}(\mathbf{k}_0)$ and $f_{2,2}(\mathbf{k}_0)$ have f -wave symmetries with 6 nodes, and the relative phase shift between the two is exactly $\delta\phi_{\mathbf{k}_0} = \pi/6$ as in two orthogonal f -wave components. Thus, the down-folded pairing interaction in the moiré bands of the twisted double-layer leads to the reconstruction of two orthogonal nodal f -wave order parameters in the moiré BZ, which provides the basis for the T -broken chiral phase. Next, we solve for $\Delta_{1,p}$ and $\Delta_{2,p}$ by minimizing the free energy density

$$\mathcal{F}_{SC} = \sum_{l,p} \frac{|\Delta_{l,p}|^2}{U_0} - \frac{1}{V} \sum_{s,\mathbf{k}_0} \frac{1}{2\beta} \ln(1 + e^{-\beta E_{s,\mathbf{k}_0}}), \quad (5)$$

where V is the volume of the system, $\beta = 1/k_B T$ (T : temperature), E_{s,\mathbf{k}_0} are the eigenvalues of \mathcal{H}_{BdG} (Eq. (4)). Given two identical layers of STVS superconductors, we have $|\Delta_{1,p}| = |\Delta_{2,p}|$, and the general solution up to an overall phase is given by $\Delta_{1,p} = \Delta_0$, $\Delta_{2,p} = \Delta_0 e^{i\varphi_p}$ where we take Δ_0 to be real. To explore the resulting phase diagram in a concrete setting we set $U_0 = 0.013t$ in Eq. (5) and $\mu = 2.9t$. With $t = 1 \text{ eV}$ this yields $T_c \approx 3K$ and $\Delta_0 \approx 1 \text{ meV}$ at $T = 0$, almost independent of θ .

The complete superconducting phase diagram in the $\mu - \theta$ space is shown in Fig. 3b. For θ in close vicinity of 30° , the system

develops a spontaneous T -broken phase characterized by $0 < \varphi_p < \pi$ and becomes an intrinsic chiral $f \pm if'$ -wave superconductor. It is noteworthy that the chiral phase persists over almost the entire chemical potential range that produces a connected FS, as shown in blue-shaded regions in Fig. 3b. At $\theta = 30^\circ$, the free energy \mathcal{F}_{SC} is minimized exactly at $\varphi_p = \pm \pi/2$ (red solid line in Fig. 3c) with $\Delta_{2,p} = \pm i\Delta_{1,p}$, which corresponds to a perfect $f \pm if'$ -wave symmetry. As θ deviates from 30° , φ_p gradually evolves towards 0 or π for $\theta \leq \theta_c^-$ and $\theta \geq \theta_c^+$, respectively (Fig. 3c), and the two layers of STVS superconductors eventually form a $0(\pi)$ -phase junction.

The bulk Bogoliubov excitation energy gaps along the circular Fermi surface at $\mu = 2.9t$ in different superconducting phases are shown in Fig. 3e-g. We find that for $\theta < \theta_c^-$ and $\theta > \theta_c^+$, the system in the T -preserving phase is a nodal f -wave superconductor with 6 nodes along the Fermi surface. While in the T -broken chiral regime, the system exhibits a full superconducting gap. In the next section, we demonstrate the nontrivial topological properties of the chiral $f \pm if'$ phase as well as the nodal f -wave SC phase by studying their boundary and vortex core excitations.

Ginzburg-Landau theory. To understand why a robust chiral $f \pm if'$ phase emerges at $\theta \approx 30^\circ$, we construct a phenomenological Ginzburg-Landau (GL) theory in terms of the reconstructed $\psi_1 \equiv \Delta_{1,p}$, $\psi_2 \equiv \Delta_{2,p}$ in moiré band p . Note that due to the reconstruction of pairing interactions in the moiré bands, the symmetry properties of ψ_1, ψ_2 , as summarized in Table 1, do not directly follow from the f -wave symmetries in each isolated layer, but need to be derived from the defining equations for the basis functions $f_{1,2}(\mathbf{k}_0)$ and $f_{2,2}(\mathbf{k}_0)$ formulated in the moiré bands (Eq. (16) in the “Mean-field gap equation for twisted double-layer STVS superconductors” in Methods section). For a general twist angle θ , the double-layer has D_6 point group symmetry, which dictates the form

Table 1 Irreducible representations (ireps) of point group D_6 ($\theta \neq 30^\circ$) and D_{6d} ($\theta = 30^\circ$).

Group	IR	cubic functions	SC order parameters
D_6	A_1	—	$\psi_1 \psi_2^* + \psi_1^* \psi_2$ $\psi_1^2 \psi_2^{*2} + \psi_1^{*2} \psi_2^2$
	B_1	$x^3 - 3xy^2$	$\psi_1 + \psi_2$
	B_2	$3x^2y - y^3$	$\psi_1 - \psi_2$
D_{6d}	A_1	—	$\psi_1^2 \psi_2^{*2} + \psi_1^{*2} \psi_2^2$
	E_3	$\{x^3 - 3xy^2, 3x^2y - y^3\}$	$\{\psi_1 + \psi_2, \psi_1 - \psi_2\}$

Basis functions include cubic functions and reconstructed f -wave superconducting (SC) order parameters ψ_1, ψ_2 in the moiré bands in twisted double-layer. Symmetry properties of ψ_1, ψ_2 are derived from Eq. (16). A_1 is the trivial irep in both cases.

of the GL free energy

$$\mathcal{F}_{\text{GL}}[\psi_1, \psi_2] = \sum_{l=1,2} \alpha_0 |\psi_l|^2 + \frac{\beta_0}{2} |\psi_l|^4 + a_0 |\psi_1|^2 |\psi_2|^2 + b_0 (\psi_1 \psi_2^* + \text{c.c.}) + c_0 (\psi_1^2 \psi_2^{*2} + \text{c.c.}) \quad (6)$$

where the coefficients b_0, c_0 characterize the coherent tunneling of single and double Cooper pairs between the layers, respectively. Taking $\psi \equiv |\psi_1| = |\psi_2|$ (see detailed analysis on the validity of this choice in Supplementary Note 4 and 5), this becomes $\mathcal{F}_{\text{GL}}(\varphi) = \mathcal{F}_0 + 2b_0 \psi^2 \cos(\varphi) + 2c_0 \psi^4 \cos(2\varphi)$, where φ is the phase difference between ψ_1 and ψ_2 , and $\mathcal{F}_0 = 2\alpha_0 \psi^2 + (\beta_0 + a_0) \psi^4$.

At the maximal twist $\theta = 30^\circ$, the twisted double-layer becomes a quasi-crystal with 12-fold tiling as discussed in the Normal-state fermiology subsection. The symmetry of the quasi-crystal is described by the non-crystallographic D_{6d} point group, which includes an extra improper rotation $S_{12} \equiv \sigma_h \otimes C_{12}$, i.e., a 12-fold rotation about the z -axis combined with the reflection about the horizontal mirror plane lying mid-way between the two layers (see Fig. 2a). We deduce that under S_{12} : $\psi_1 \rightarrow -\psi_2, \psi_2 \rightarrow \psi_1$. For the GL free energy in Eq. (6) to be invariant under S_{12} , the single-pair tunneling term must vanish: $b_0 = 0$, and the only φ -dependent term is proportional to coefficient c_0 and exhibits $\cos(2\varphi)$ dependence. As argued in the twisted cuprate case, the coefficient c_0 associated with the double-pair tunneling is generally positive. In Supplementary Note 4 we further verify that $c_0 > 0$ generally holds in the case of twisted STVS superconductors by expanding the microscopic free energy Eq. (5) in terms of $\Delta_{1,2}$ and $\Delta_{2,2}$ using the imaginary-time path integral formalism. Thus, the quasi-crystalline D_{6d} symmetry dictates that the free energy is always minimized for $\varphi_{\text{min}} = \pm \pi/2$ implying a state with spontaneously broken \mathcal{T} -symmetry.

The distinctive quasi-crystalline D_{6d} point group at $\theta = 30^\circ$ has important consequences for the temperature dependence of the chiral $f \pm if'$ phase. It is worth noting that by construction for general θ (Fig. 2a-b), the basis functions $f_1(\mathbf{k}_0)$ and $f_2(\mathbf{k}_0)$ are always symmetric about the $\mathbf{k}_{0,y} = 0$ axis when $\phi_{\mathbf{k}_0} = 0, \pi$, and anti-symmetric about $\mathbf{k}_{0,x} = 0$ when $\phi_{\mathbf{k}_0} = \pm \pi/2$ (see Fig. 3a). As such, the $\varphi = 0$ phase is essentially the $f_{x(x^2-3y^2)}$ pair function formed by the real combination $f_1(\mathbf{k}_0) + f_2(\mathbf{k}_0) \propto k_{x,0}(k_{x,0}^2 - 3k_{y,0}^2)$, which belongs to the 1D irreducible representation (irep) of D_6 labeled B_1 in Table 1. On the other hand, the $\varphi = \pi$ phase corresponds to the $f_{y(3x^2-y^2)}$ pair function formed by an orthogonal real linear combination $f_1(\mathbf{k}_0) - f_2(\mathbf{k}_0) \propto k_{y,0}(3k_{x,0}^2 - k_{y,0}^2)$, which belongs to another 1D irep of D_6 labeled B_2 . Thus, for θ away from 30° , the two phases belonging to distinct ireps of D_6 have different ground state energies (see free energy landscapes at $T=0$ in Fig. 3c for $\theta \neq 30^\circ$) and correspond to different T_c .

At $\theta = 30^\circ$, however, the two orthogonal f -wave states with $\varphi = 0$ and $\varphi = \pi$ are degenerate (see free energy landscape in Fig. 3c for $\theta = 30^\circ$), and form a 2D representation of D_{6d} , labeled E_3 in Table 1, with both components having the same T_c . Accordingly, as shown in the $T - \theta$ phase diagram Fig. 3d, obtained by minimizing \mathcal{F}_{SC} at finite T , the chiral $f \pm if'$ phase extends all the way to $T = T_c$ for $\theta = 30^\circ$ because both orthogonal f -wave components condense simultaneously when superconductivity sets in at T_c . For θ away from 30° , the component with higher T_c (either $\varphi = 0$ or $\varphi = \pi$) sets in first, and one needs to further lower the temperature to access the other orthogonal component with lower T_c to form the chiral $f \pm if'$ phase.

In the zero-temperature limit, the chiral $f \pm if'$ phase extends between critical angles $\theta_c^- \simeq 29.7^\circ - 29.8^\circ$ and $\theta_c^+ \simeq 30.2^\circ - 30.3^\circ$ (Fig. 3b-d). The overall twist angle range of $\delta\theta \simeq 0.4 - 0.6^\circ$ is well within reach of twist angle engineering precision $\sim 0.1^\circ$ now common in the state-of-the-art sample fabrication technique for twisted materials^{22,23,25-27}. We note that the twist angle range predicted here is narrower than the chiral $d \pm id'$ phase found in twisted cuprates which can span several degrees³⁰. As we explain in Supplementary Note 6, the relatively narrow twist angle range originates from the nontrivial θ -dependence of the reciprocal lattice vectors $\tilde{\mathbf{G}}_m, \mathbf{G}_n$, for $m, n \neq 0$ that determine the interlayer coupling strength, as opposed to the coupling dominated by $\tilde{\mathbf{G}}_0 = \mathbf{G}_0 = \mathbf{0}$ in cuprates which is, to good approximation, θ -independent.

Nodal topological f -wave phase. As we discussed in previous sections, for $\theta < \theta_c^-$ ($\theta > \theta_c^+$), the twisted double-layer favors the $\varphi = 0$ ($\varphi = \pi$) phase and becomes a nodal $f_{x(x^2-3y^2)}$ -wave ($f_{y(3x^2-y^2)}$ -wave) superconductor. This nodal phase is topologically nontrivial in the sense that the f -wave nodes are characterized by chirality numbers⁴⁹, and, in a geometry with edges, nodes of opposite chirality are connected by protected non-dispersive Majorana edge modes.

To understand the nontrivial topological property of the nodal f -wave phase, we consider the specific case with $\theta = 29.5^\circ$ and $\varphi = 0$ in band $p = 2$ corresponding to Fig. 3e. In the Nambu basis $\psi(\mathbf{k}_0) = \left(a_2(\mathbf{k}_0), a_2^\dagger(\mathbf{k}_0) \right)^T$, the bulk BdG Hamiltonian is written as $\mathcal{H}_{\text{BdG}} = \sum_{\mathbf{k}_0} \psi^\dagger(\mathbf{k}_0) H_{\text{BdG}}(\mathbf{k}_0) \psi(\mathbf{k}_0)$, where $H_{\text{BdG}}(\mathbf{k}_0) = \xi_2(\mathbf{k}_0) \tau_3 + \Delta_2(\mathbf{k}_0) \tau_1$ with $\tau_{\alpha=1,2,3}$ as Pauli matrices acting on particle-hole space, and $\Delta_2(\mathbf{k}_0) = \Delta_0(f_{1,2}(\mathbf{k}_0) + f_{2,2}(\mathbf{k}_0))$.

The Hamiltonian H_{BdG} respects a chiral symmetry $\mathcal{C} H_{\text{BdG}} \mathcal{C}^{-1} = -H_{\text{BdG}}$ where $\mathcal{C} = \tau_2$. It can be represented in the eigenbasis of \mathcal{C} , by translating $\tau_3 \mapsto \tau_1, \tau_1 \mapsto \tau_2$. Then, in the vicinity of a nodal point $\mathbf{k}_{0,N}$, the excitations can be described as 2D massless Dirac fermions

$$h_N(\mathbf{p}_0) \simeq v_1 p_{0,1} \tau_1 + v_2 p_{0,2} \tau_2, \quad (7)$$

where $p_{0,1}$ and $p_{0,2}$ denote the normal and tangential components along the Fermi surface of a momentum $\mathbf{p}_0 = \mathbf{k}_0 - \mathbf{k}_{0,N}$. Dirac velocities $v_1 \equiv \nabla_{\mathbf{k}_0} \xi_2(\mathbf{k}_0) \cdot \hat{\mathbf{n}}_1$ and $v_2 \equiv \nabla_{\mathbf{k}_0} \Delta_2(\mathbf{k}_0) \cdot \hat{\mathbf{n}}_2$ are evaluated at $\mathbf{k}_0 = \mathbf{k}_{0,N}$. The chirality at $\mathbf{k}_{0,N}$ can then be defined as $C(\mathbf{k}_{0,N}) = \text{sgn}(v_1 v_2) \hat{\mathbf{z}} \cdot (\hat{\mathbf{n}}_1 \times \hat{\mathbf{n}}_2)$.

The chiralities $C(\mathbf{k}_{0,N})$ of the 6 nodes in the $\varphi = 0$ phase are calculated from $H_{\text{BdG}}(\mathbf{k}_0)$ and indicated in Fig. 4a. Clearly, nodes with opposite chiralities come in three pairs, reflecting the underlying $f_{x(x^2-3y^2)}$ -symmetry. It is worth noting that by projecting the bulk spectrum onto the edges oriented along certain high-symmetry directions, e.g. the y -direction, nodes with opposite chiralities do not cancel out. In this situation we expect protected non-dispersive edge modes to appear in

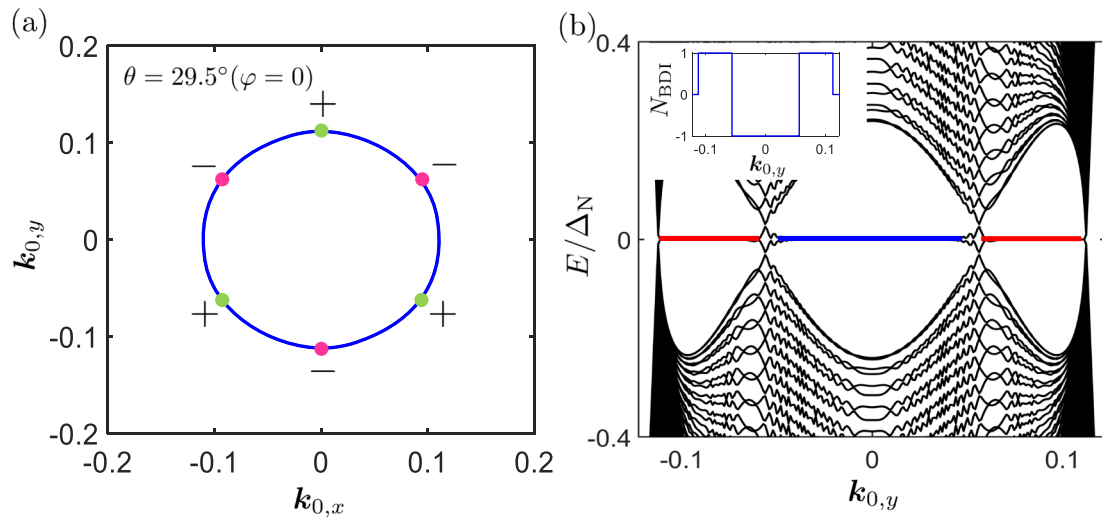


Fig. 4 Nontrivial topology of the nodal f -wave phase. **a** Locations of f -wave nodes in the momentum space of $\mathbf{k}_0 = (k_{0,x}, k_{0,y})$. Chiralities of nodes indicated by “ \pm ” signs in the $\varphi = 0$ phase with $f_{x(x^2-3y^2)}$ -wave pairing symmetry. **b** Edge spectrum of the Bogoliubov-de-Gennes (BdG) Hamiltonian H_{BdG} with phase difference $\varphi = 0$ in a strip geometry as a function of $k_{y,0}$ along edges oriented in the y -direction, calculated using the lattice model in Eq. (8)–(9) with $\Delta_{\text{NN}} = 0$ such that only the $f_{x(x^2-3y^2)}$ -wave component is present. Inset: Nontrivial topology of nodal f -wave phase is characterized by the BDI invariant N_{BDI} as a function of $k_{y,0}$ (see Supplementary Note 7). The regions with $N_{\text{BDI}} = +1$ (-1) correspond to regions with Majorana zero modes (MZMs) highlighted in red (blue) in (b). $k_{0,x}, k_{0,y}$ are given in units of \AA^{-1} .

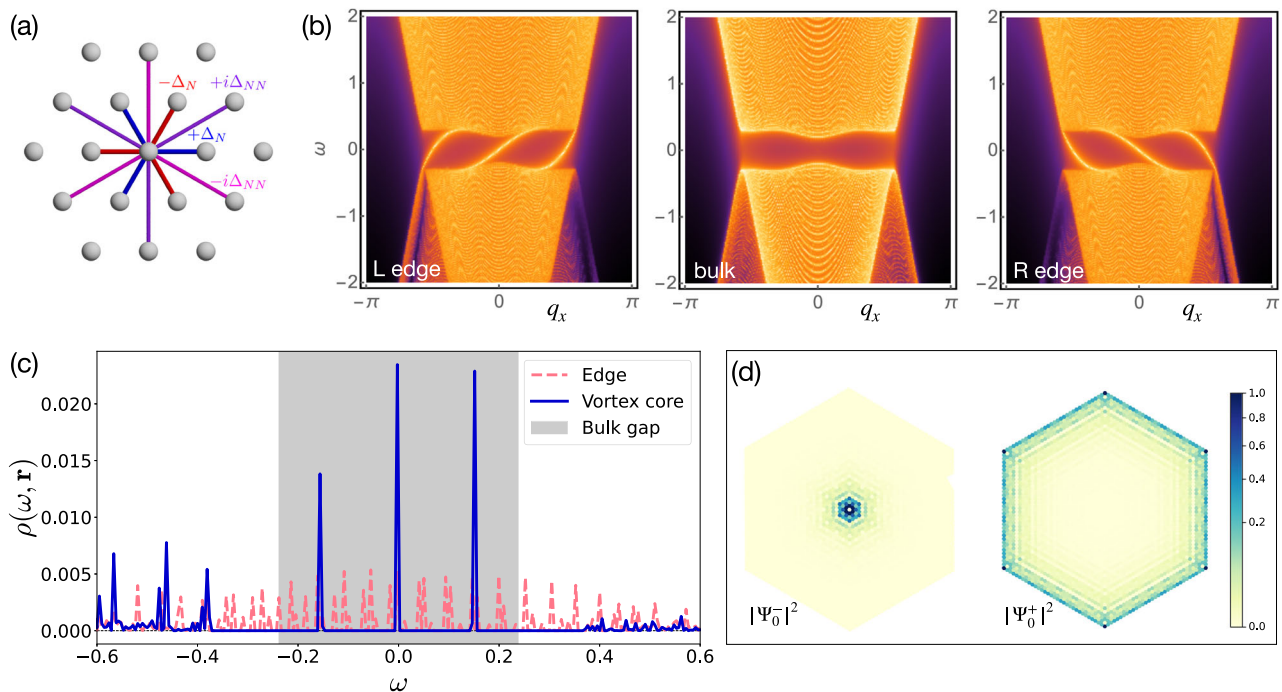


Fig. 5 Exact diagonalization results for edge and vortex core Majorana modes. **a** Pairing amplitudes for the f -wave order parameter on the simplified triangular lattice model with lattice constant a_0 . Δ_N and Δ_{NN} denote the nearest-neighbor and second-nearest-neighbor pairing amplitudes, respectively. **b** Spectral function $A(q_x, \omega)$ evaluated at the edges and in the bulk of an infinite strip with width of $L = 200$ sites. ω is shown in units of t_0 . **c** Local density of states $\rho(\omega, \mathbf{r})$ computed on a hexagon-shaped sample with $N = 3169$ sites and a vortex located at its center. **d** Real-space probability distribution of zero-energy eigenstates $|\Psi_0^\pm\rangle = (\Psi_0 \pm \Psi'_0)/\sqrt{2}$. The color bar indicates the normalized value of probability distribution to the maximum site amplitude for each state. In all panels parameters $(\mu_0, \Delta_N, \Delta_{\text{NN}}) = (0.8t_0, 0.5t_0, \Delta_N/3\sqrt{3})$ with $t_0 = -0.01$ eV were used.

analogy with the flat bands on zigzag edges of monolayer graphene⁴².

To demonstrate the existence of edge states in the nodal f -wave phase, we now introduce a simplified triangular lattice model with lattice constant a_0 (shown schematically in Fig. 5a) for band $p = 2$ derived from the DMSTB model above (Fig. 2d). The lattice model captures both the parabolic dispersion near Γ

and the f -wave pairing symmetry, thus facilitating explicit calculations of edge states as well as vortex excitations of the chiral superconductor presented below. The lattice model is defined by

$$\mathcal{H}_{\text{LAT}} = \sum_{\mathbf{q}} \left[\xi_{\mathbf{q}} c_{\mathbf{q}}^\dagger c_{\mathbf{q}} + (\Delta_{\mathbf{q}} c_{\mathbf{q}}^\dagger c_{-\mathbf{q}}^\dagger + \text{h.c.}) \right], \quad (8)$$

where $\xi_{\mathbf{q}} = -2t_0 \sum_{j=1,3,5} \cos(\mathbf{q} \cdot \boldsymbol{\delta}_j) - \mu_0$ denotes the band energy from effective electron hopping $-t_0$, where we set $t_0 \simeq 0.01t$ by fitting the parabolic dispersion at Γ in Fig. 2d. The gap function is given by

$$\Delta_{\mathbf{q}} = 2 \sum_{j=1,3,5} \left[\Delta_N \sin(\mathbf{q} \cdot \boldsymbol{\delta}_j) + i\Delta_{\text{NN}} \sin(\mathbf{q} \cdot \boldsymbol{\delta}'_j) \right] \quad (9)$$

with Δ_N (Δ_{NN}) denoting the first (second) nearest-neighbor pairing amplitudes as shown in Fig. 5a, while $\boldsymbol{\delta}_j$ and $\boldsymbol{\delta}'_j$ are the corresponding bond vectors indicated by red and purple lines, respectively. It is straightforward to check that in the small \mathbf{q} expansion, the two pairing terms produce two orthogonal $f_{x(x^2-3y^2)}$ - and $f_{y(3x^2-y^2)}$ -wave components, respectively.

We use the lattice model in Eq. (8) with $\Delta_{\text{NN}} = 0$ to calculate the edge spectrum of the nodal $f_{x(x^2-3y^2)}$ -wave superconductor as a function of $k_{0,y}$ (Fig. 4b), where we identify $k_{0,y}$ as q_y in Eq. (8)–(9). As anticipated the bulk nodes with opposite chiralities are connected by non-dispersive zero energy modes on the edge (highlighted by red and blue lines in Fig. 4b). As we explain in Supplementary Note 7, for each fixed $k_{0,y}$, $H_{\text{BdG}}(k_{0,x})$ describes a one-dimensional BDI class topological superconductor oriented in the x -direction, with its topological property characterized by a winding number $N_{\text{BDI}}^{40,50,51}$ (inset of Fig. 4b). The bulk-edge correspondence between N_{BDI} and the number of zero energy modes allows us to establish the edge state associated with each $k_{y,0}$ as a MZM. We note that as long as the chiral symmetry \mathcal{C} is respected, chiralities of nodes are well defined and act as topological charges that only annihilate when opposite charges merge in the bulk. Therefore, the large number of non-dispersive MZMs on the edge are protected by the nontrivial bulk topology against \mathcal{C} -preserving perturbations such as charge disorder^{52–55}.

Majorana modes in chiral $f \pm if'$ phase. In the \mathcal{T} -broken $f \pm if'$ phase, that we shall model by the lattice Hamiltonian Eq. (8) with $\Delta_{\text{NN}} \neq 0$, the 6 Dirac nodes are gapped out by alternating mass terms produced by the imaginary $f_{y(3x^2-y^2)}$ -wave component of the order parameter. This gapped phase belongs to symmetry class D in Altland-Zirnbauer classification^{40,50,51} and its topology is therefore characterized by the Chern number C . In analogy with the $d + id'$ phase in cuprates we expect each gapped Dirac point to contribute $\frac{1}{2} \text{sgn}(\Delta_{\text{NN}})$ to the total Chern number, suggesting that the system will have $C = \pm 3$ in the gapped chiral phase. Because the BdG representation of the spinless superconductor is redundant, the Chern number here determines the number of chiral Majorana edge modes with central charge 1/2 (as opposed to complex fermion modes whose central charge would be 1).

We can now confirm the existence of edge states by placing \mathcal{H}_{LAT} on a strip geometry with periodic boundary conditions in the x -direction, and L rows of atoms in the y -direction. The spectral function in 1D momentum space, plotted in Fig. 5b, allows us to visualize the excitations present in each row of the strip. It is defined as

$$A(q_x, \omega) = \text{Im}[(\omega + i\eta) - \mathcal{H}_{\text{LAT}}(q_x)]^{-1} \quad (10)$$

where η is a positive infinitesimal, and $\mathcal{H}_{\text{LAT}}(q_x)$ is the $L \times L$ Hamiltonian on the strip with q_x the lattice momentum along x . The spectral function reveals a fully gapped bulk and three distinct edge modes traversing the bulk gap, propagating in opposite directions at each edge. This confirms the Chern number $C = 3$ deduced above from general considerations.

In addition to gapless edge modes, chiral p -wave superconductors threaded with unit magnetic flux are predicted to host unpaired MZMs obeying non-Abelian exchange statistics, which are localized at vortex cores^{7,8}. To model the effect of an

Abrikosov vortex in the $f + if'$ superconductor, we adopt a real-space representation of the lattice model in Eq. (8). We consider a hexagonal domain with open boundary conditions, and place a vortex at the origin. This induces a phase winding on the order parameter for each bond

$$\begin{aligned} \Delta_{\mathbf{r},\boldsymbol{\delta}_j} &= (-1)^{j-1} \Delta_N \exp(-in\theta_{\mathbf{r},\boldsymbol{\delta}_j}) \\ \Delta_{\mathbf{r},\boldsymbol{\delta}'_j} &= (-1)^{j-1} \Delta_{\text{NN}} \exp(-in\theta_{\mathbf{r},\boldsymbol{\delta}'_j}) \end{aligned} \quad (11)$$

where \mathbf{r} denote lattice sites in real-space; n is the vorticity; and $\theta_{\mathbf{r},\boldsymbol{\delta}_j}$ is the angle subtended by the midpoint of the bond $(\mathbf{r} + \frac{1}{2}\boldsymbol{\delta}_j)$, the origin, and the x -axis. We then numerically diagonalize the $2N \times 2N$ matrix representing \mathcal{H}_{LAT} , where N is the number of lattice sites.

For a single-quantum vortex solution with $n = 1$, we indeed find a single zero-energy mode, which manifests as a zero-bias peak in the local density of states (LDOS) at the vortex core. Its partner lives at the sample edge, as shown in Fig. 5c. The LDOS is given by

$$\rho(\omega, \mathbf{r}) = \sum_{E_n > 0} \{ |u_n(\mathbf{r})|^2 \delta(\omega - E_n) + |v_n(\mathbf{r})|^2 \delta(\omega + E_n) \} \quad (12)$$

where E_n are eigenvalues of \mathcal{H}_{LAT} with eigenstates $\Psi_n(\mathbf{r}) = (u_n(\mathbf{r}), v_n(\mathbf{r}))^T$. To confirm the nature of the two zero-energy states, denoted Ψ_0 and Ψ'_0 , we plot their real-space wavefunctions in Fig. 5d. The symmetric and anti-symmetric linear combination of these states are self-conjugate eigenstates of the charge conjugation operator, and represent Majorana zero modes localized at the sample edge and vortex core, respectively.

Discussion

Here we discuss how the exotic non-Abelian TSC phase can be realized in twisted double layers formed by the promising candidate materials, rhombohedral graphene^{34,35} and ZrNCl³⁸, which are thought to be STVS superconductors. It is worth noting that the spinless-fermion triangular lattice model used for our theoretical considerations captures most of the essential features of the spin-triplet SC2 phase in rhombohedral trilayer graphene (RTG): (i) the SC2 phase emerges under strong displacement fields which polarize the layer and sublattice degrees of freedom, such that electrons involved in superconducting pairing actually live on an effective triangular lattice formed by the A (or B) sublattice³⁵; (ii) the Fermi surface of the parent spin-polarized valley-unpolarized normal state underlying the SC2 phase is well reproduced by our model (Fig. 2).

To realize the topological phase with non-Abelian excitations, it is crucial that the isolated K -pockets from each layer coalesce into a single connected Fermi surface in the moiré Brillouin zone. Our results based on the DMSTB model suggest that a minimal Fermi momentum $k_{\text{Fa}} \sim 0.2$ ($a = 2.46 \text{ \AA}$ for graphene) measured from $\pm K(\tilde{K})$ is required for a single connected Fermi surface to emerge (see Fig. 2f). The typical value of Fermi momentum in RTG, corresponding to a low doping level with carrier density $n_{2\text{D}} \approx 0.5 \times 10^{12} \text{ cm}^{-2}$, was found to be of order $k_{\text{Fa}} \sim 0.1$ ³⁴, which is almost on par with the minimal requirement according to our theory. We note that higher doping levels, up to $n_{2\text{D}} \sim 1 \times 10^{12} \text{ cm}^{-2}$, are indeed accessible through electrostatic gating^{34,35}, and the non-Abelian topological superconductivity could thus be achieved by further raising the doping level in maximally twisted double-layer RTG.

The triangular lattice model also captures the parabolic dispersion near $\pm K$ of the doped band insulator ZrNCl^{56,57} and was in fact used to study the STVS pairing³⁸. In particular, ZrNCl superconducts within a wide range of electron doping $x \sim 0.01 - 0.3$ ^{58–60} (x : number of electrons per unit cell). The

simple parabolic dispersion near $\pm K$ allows us to extract a Fermi momentum $k_F a = \sqrt{x\pi} \simeq 0.2 - 1.0$ with lattice constant $a = 3.663 \text{ \AA}$ for ZrNCl, which suggests that the condition for a single connected FS in maximally twisted double-layer is readily fulfilled.

The f -wave pairing interaction in the non-magnetic ZrNCl may generally involve all three triplet channels given its spin-degenerate band structure, with the spinor part of the pair function characterized by a three-component \mathbf{d} -vector $\Delta_i = (\mathbf{d} \cdot \boldsymbol{\sigma})i\sigma_y$ ($\sigma_{\alpha=x,y,z}$: Pauli matrices for spins). Given the D_6 -point group of the twisted double-layer, however, the doublet formed by equal-spin states $\{|\uparrow\uparrow\rangle, |\downarrow\downarrow\rangle\}$ and the anti-parallel state $|\uparrow\downarrow\rangle + |\downarrow\uparrow\rangle$ will in general be distinct in energies as they belong to different E_1 and A_2 irreps of D_6 , respectively. In the E_1 phase with a two-component order parameter $\mathbf{d} = (d_x, d_y, 0)$, the total BdG Hamiltonian is decomposed into two independent spin sectors, each one described by the spinless model discussed in this work. Thus, our analysis directly applies and the system near the maximal twist becomes a spinful chiral $f \pm if'$ superconductor. As degrees of freedom are doubled, there would be two species of chiral Majorana modes on the edge corresponding to three complex fermions; as well as two MZMs, one from each spin sector, localized at the single-vortex core. It is worth noting, however, as the two-component \mathbf{d} -vector can rotate around the vortex core, the spinful chiral $f \pm if'$ state admits half-quantum vortex (HQV) solutions trapping a π -flux. Following the analysis developed for spinful chiral p -wave superconductors in the context of Sr_2RuO_4 and $^3\text{He-A}$ phase^{7,61}, the HQV is equivalent to a single-quantum vortex in one of the effective spin sectors and thus hosts a non-Abelian MZM.

In obtaining the phase diagrams in Fig. 3, we considered a relatively strong pairing interaction which yields a native $T_c \simeq 3K$ and sizable pairing amplitude $\Delta_0 \simeq 1 \text{ meV}$ for the twisted double-layer. While such temperature and energy scales are directly relevant to ZrNCl⁶⁰, the spin-triplet superconductivity in RTG and BBG is found with a much lower $T_c \simeq 50 \text{ mK}$ ^{34,35}. It is important to note, however, that the emergence of the chiral $f \pm if'$ phase follows from general symmetry principles as illustrated in our Ginzburg-Landau analysis. The proposed mechanism should therefore be largely insensitive to microscopic details and remains applicable to RTG and BBG. We further note that phase diagrams in Fig. 3 do not change qualitatively when the inter-layer coupling strength is varied, as long as it remains on the scale of $t_{\perp}(K) \sim 0.1t$. For weaker interlayer coupling, $t_{\perp}(K) \lesssim 0.01t$, the energy bands become dense in energy space and the parameter regime with a single connected Fermi surface in Fig. 3b is reduced.

To detect the \mathcal{T} -broken chiral $f \pm if'$ phase a suite of spectroscopic and transport experiments proposed for the chiral $p + ip'$ and $d + id'$ phases in Sr_2RuO_4 and twisted cuprates can be applied. The nonzero orbital angular momentum $L_z = \pm 3$ in the chiral $f \pm if'$ phase can be probed by polar Kerr effect measurements^{62,63}, and the two-minimum free energy landscape near $\theta = 30^\circ$ shown in Fig. 3c will give rise to anomalous π -periodic inter-layer Josephson current-phase relation $I_J = (2e/\hbar)\partial\mathcal{F}_{\text{SC}}/\partial\varphi \propto \sin(2\varphi)$ ³⁰. Upon tuning θ and T , the transition from fully gapped chiral phase to nodal f -wave phase (Fig. 3d-h) can be detected by a change from U -shaped to V -shaped spectra in the bulk LDOS, which can be probed by scanning tunneling microscopy (STM) measurements⁶⁴. Moreover, STM can be used to detect and resolve the spatial profile of the zero bias peaks induced by the MZM localized at the vortex core^{16,17}, as well as the non-dispersive edge MZMs in the nodal f -wave phase.

Conclusions

We established an avenue through twist-angle engineering toward intrinsic chiral $f \pm if'$ TSC with non-Abelian excitations. In

particular, the emergence of non-Abelian TSC in maximally twisted STVS superconductors relies on a special type of large-angle moiré physics which is absent in twisted cuprates and is fundamentally different from the moiré physics in small-angle twisted graphene (see detailed comparison between these systems in Supplementary Note 1). Our Ginzburg-Landau analysis reveals that the energetics leading to the exotic chiral $f \pm if'$ phase are governed by a non-crystallographic D_{6d} symmetry, which emerges generically in the 12-fold quasi-crystalline structure formed at 30° twist. By virtue of adiabatic continuity we expect the gapped topological phase to persist in a finite range $\delta\theta$ of twist angles around 30° and our microscopic model indeed indicates stability for $\delta\theta \simeq 0.4^\circ - 0.6^\circ$, well within the capability of current sample fabrication techniques. We note that the possibility of chiral $f \pm if'$ pairing was also suggested in a recent work on high-angular momentum-superconductivity in large-angle-twisted homobilayer systems⁶⁵.

The proposed mechanism applies in general to any two-valley material with hexagonal symmetry that exhibits gapped f -wave superconductivity in its monolayer form. The formation of a single connected FS in the twisted double-layer - an important prerequisite for non-Abelian excitations - requires states from the two different valleys $\pm K(\pm \bar{K})$ to hybridize (Fig. 2c-h). Therefore, the large-angle moiré physics necessarily violates the fundamental valley conservation symmetry $U_v(1)$ that underpins the well-established moiré physics in small-angle-twisted graphene and transition-metal dichalcogenides. This provides an alternative symmetry perspective on why the BM-type continuum models applicable in the small-angle limit, in which the $U_v(1)$ is built-in by construction, fail to describe the moiré physics at maximal twist. As we discuss in detail in Supplementary Note 1, the $U_v(1)$ -violation in maximally twisted double-layer is crucial for non-Abelian TSC because any description respecting the $U_v(1)$ symmetry cannot support a single unpaired non-Abelian Majorana mode in a zero-momentum-paired superconductor, regardless of its pairing symmetry. This $U_v(1)$ -based criterion reveals a profound connection between the large-angle moiré physics established in this work and \mathcal{T} -broken non-Abelian TSC.

While our assumption of a dominant pairing interaction in the f -wave channel for spin-triplet SC2 phase of RTG/BBG is supported by proposals based on acoustic phonons^{36,37} and renormalization group analysis⁶⁶, some recent works suggest an alternative possibility of chiral $p \pm ip'$ pairing symmetry⁶⁷⁻⁶⁹, which is also compatible with the phenomenology of the SC2 phase. In Supplementary Note 8 we present a detailed analysis of pairing instabilities in all possible pairing channels in maximally twisted double-layer RTG/BBG. Our microscopic calculations reveal that the chiral f -wave phase takes up the vast majority of the superconducting phase diagram, which lends strong support to the central idea developed in this work. In particular, we find that the chiral p -wave phase is favored only when the p -wave coupling constant is overwhelmingly larger than the coupling constant in the f -wave channel.

Our detailed calculations in addition show that under a dominant chiral p -wave interaction, the superconducting free energy and inter-layer Josephson current at $\theta = 30^\circ$ exhibits a 2π -periodicity in its φ -dependence, as opposed to the anomalous π -periodic dependence in the case of f -wave pairing (see Fig. 3c and Fig. S5 in Supplementary Note 8). These two contrasting behaviors can serve as experimental signatures discriminating between f -wave and chiral p -wave order parameters proposed for the SC2 phase in RTG. These results suggest potential applications of large-twist-angle engineering in probing the pairing symmetries of unconventional superconductors.

While the exact nature of the pairing symmetry of the SC2 spin-triplet phase remains to be settled by future experiments, it is

important to note that even under the topological chiral $p \pm ip'$ pairing symmetry, an isolated monolayer still cannot support non-Abelian excitations due to the disconnected nature of its Fermi surface. On the other hand, maximally twisted double layer favors a configuration with the same p -wave chiralities in both layers. The resulting composite system then becomes a standard spinless chiral $p \pm ip'$ superconductor hosting non-Abelian MZMs when the disconnected FS in each layer coalesce into a single FS – a detailed discussion of this is given in Supplementary Note 8. Thus, the alternative assumption of chiral p -wave pairing does not alter our conclusion that a maximal twist is required to turn the system into a non-Abelian topological phase, which further fortifies the connection between the relatively unexplored large-angle moiré physics and non-Abelian topological superconductivity.

Methods

Dual momentum-space tight-binding (DMSTB) model. Here we briefly outline the basic idea behind our generalized DMSTB model and present a detailed derivation in Supplementary Note 3.

The DMSTB model is rooted in the observation that for any given momentum \mathbf{k}_0 , the sets of Bloch states involved in the inter-layer coupling Hamiltonian Eq. (2) are $S_1(\mathbf{k}_0) = \{|\mathbf{k}_0 + \mathbf{G}, 1\rangle, \forall \mathbf{G}\}$ in layer 1, and $S_2(\mathbf{k}_0) = \{|\mathbf{k}_0 + \mathbf{G}, 2\rangle, \forall \mathbf{G}\}$ in layer 2. By viewing the Bloch states $|\mathbf{k}_m = \mathbf{k}_0 + \tilde{\mathbf{G}}_m, 1\rangle \in S_1(\mathbf{k}_0)$ and $|\tilde{\mathbf{k}}_n = \mathbf{k}_0 + \mathbf{G}_n, 2\rangle \in S_2(\mathbf{k}_0)$ as “Wannier orbitals” localized at the dual momentum-space lattice sites \mathbf{k}_m and $\tilde{\mathbf{p}}_n \equiv \mathbf{k}_0 - \tilde{\mathbf{k}}_n \equiv -\mathbf{G}_n$, the inter-layer coupling in Eq. (2) can be regarded as ‘inter-site hopping’ between \mathbf{k}_m and $\tilde{\mathbf{p}}_n$ with ‘hopping strength’ $t_{\perp, mn}(\mathbf{k}_0) = t_{\perp}(\mathbf{k}_m - \tilde{\mathbf{p}}_n)$ determined precisely by the geometric distance $|\mathbf{k}_m - \tilde{\mathbf{p}}_n|$ (see Supplementary Note 3). The rapidly decaying character of $t_{\perp}(\mathbf{q})$ implies weak hybridization among Wannier orbitals (Bloch states) at \mathbf{k}_m and $\tilde{\mathbf{p}}_n$, and states in the twisted double-layer live predominantly only on a small number of \mathbf{k}_m and $\tilde{\mathbf{p}}_n$ points. Thus, there exists an approximately closed finite subspace over which an effective Hamiltonian $\mathcal{H}_{0, \text{eff}}$ can be constructed and the mapping from \mathbf{k}_0 to the set of eigenvalues $E_p(\mathbf{k}_0)$ (p : band index) of $\mathcal{H}_{0, \text{eff}}(\mathbf{k}_0)$ then defines the band structure and the Fermi surface reformulated in the \mathbf{k}_0 -space.

For $\theta \approx 30^\circ$, states near $\pm K(\bar{K})$ in layer 1 (2) (Fig. 2b) are well covered by the 12 dual momentum-space lattice points $\mathbf{k}_m, m = 1, 2, \dots, 6$ and $\tilde{\mathbf{p}}_n, n = 1, 2, \dots, 6$ indicated in Fig. 2c. This motivates us to consider $\mathcal{H}_{0, \text{eff}}(\mathbf{k}_0)$ which includes these 12 sites together with leading-order corrections from their nearest-neighboring points $\mathbf{k}_m, \tilde{\mathbf{p}}_n$ with $m, n = 0, 7, \dots, 12$ as illustrated in Fig. 2c. As further justified in Supplementary Note 3, the leading nearest-neighbor hopping terms between $\mathbf{k}_m, \tilde{\mathbf{p}}_n$ in such approximation scheme accounts exactly for the leading-order inter-layer terms depicted in Fig. 2b. The effective normal-state Hamiltonian of a near- 30° -twisted double-layer then reads $\mathcal{H}_{0, \text{eff}} = \sum_{\mathbf{k}_0} \mathcal{H}_0(\mathbf{k}_0)$ with

$$\begin{aligned} \mathcal{H}_0(\mathbf{k}_0) = & \sum_{m=0}^{12} \xi_1(\mathbf{k}_m) c_1^\dagger(\mathbf{k}_m) c_1(\mathbf{k}_m) \\ & + \sum_{n=0}^{12} \xi_2(\tilde{\mathbf{k}}_n) c_2^\dagger(\tilde{\mathbf{k}}_n) c_2(\tilde{\mathbf{k}}_n) \\ & - \sum_{m, n=0}^{12} \left[t_{\perp}(\mathbf{k}_m - \tilde{\mathbf{p}}_n) c_1^\dagger(\mathbf{k}_m) c_2(\tilde{\mathbf{k}}_n) + \text{h.c.} \right]. \end{aligned} \quad (13)$$

To verify that $\mathcal{H}_{0, \text{eff}}$ in Eq. (13) provides an accurate description of the normal-state fermiology near the maximal twist, we note that the approach above applies to any twist angle close to 30° , including commensurate twist angles where the bilayer forms a periodic moiré superlattice and the band structure can be computed exactly via a real-space lattice model. As a convenient test case we consider commensurate angle $\theta_c = 2\sin^{-1}(\sqrt{3}/(2\sqrt{13})) \approx 27.8^\circ$ which gives rise to a moiré unit cell with 26 sites. As we demonstrate in Supplementary Note 3, \mathbf{k}_0 becomes exactly the crystal momentum at θ_c , and $\mathcal{H}_{0, \text{eff}}$ reproduces the electronic bands of the moiré lattice model with excellent accuracy. We further note that the summation over \mathbf{k}_0 in Eq. (13) should be restricted to within an area the size of the moiré Brillouin zone at $\theta = \theta_c$ to avoid over-counting of the degrees of freedom.

We further note that inter-layer spatial displacements between two layers due to angular twist can generally introduce nonzero phases in the inter-layer tunneling term in Eq. (13)^{24,46}. As we explain in Supplementary Note 9, such phases cancel out in the total phase of Cooper pairs due to the spinless time-reversal symmetry T' and thus do not affect our analysis on the superconducting phase.

Mean-field gap equation for twisted double-layer STVS superconductors. To derive the mean-field gap equations for the twisted double-layer, we first rewrite the total interaction $\mathcal{V}_{\text{tot}} = \mathcal{V}^{(1)} + \mathcal{V}^{(2)}$ in the band basis. Note that the fermionic

operator creating an electron at \mathbf{k}_0 in band p is given by

$$a_p^\dagger(\mathbf{k}_0) = \sum_m u_{pm}(\mathbf{k}_0) c^\dagger(\mathbf{k}_m) + \sum_n u_{pn}(\mathbf{k}_0) c^\dagger(\tilde{\mathbf{k}}_n), \quad (14)$$

where the coefficients $u_{pm}(\mathbf{k}_0), u_{pn}(\mathbf{k}_0)$ can be found by exact numerical diagonalization of $\mathcal{H}_{0, \text{eff}}$ in Eq. (13). Fermionic operators in $\mathcal{V}^{(1)}$ and $\mathcal{V}^{(2)}$ can be rewritten as $c^\dagger(\mathbf{k}_m) = \sum_p u_{mp}^*(\mathbf{k}_0) a_p^\dagger(\mathbf{k}_0)$, $c^\dagger(\tilde{\mathbf{k}}_n) = \sum_p u_{np}^*(\mathbf{k}_0) a_p^\dagger(\mathbf{k}_0)$. Using the one-to-one correspondence $\mathbf{k}_m \equiv \mathbf{k}_0 + \tilde{\mathbf{G}}_m$ and $\tilde{\mathbf{k}}_n \equiv \mathbf{k}_0 + \mathbf{G}_n$, the pairing interaction in the band basis becomes

$$\mathcal{V}_{\text{eff}} = -U_0(F_1^\dagger F_1 + F_2^\dagger F_2), \quad (15)$$

where $F_l^\dagger \equiv \sum_{\mathbf{k}_0, p} f_{l,p}(\mathbf{k}_0) a_p^\dagger(\mathbf{k}_0) a_p^\dagger(-\mathbf{k}_0)$ is the pair creation operator in layer $l = 1, 2$, with

$$\begin{aligned} f_{1,p}(\mathbf{k}_0) &= \sum_m \Lambda_{m,p}(\mathbf{k}_0) f_1(\mathbf{k}_0 + \tilde{\mathbf{G}}_m), \\ f_{2,p}(\mathbf{k}_0) &= \sum_n \Lambda_{n,p}(\mathbf{k}_0) f_2(\mathbf{k}_0 + \mathbf{G}_n). \end{aligned} \quad (16)$$

Here, $\Lambda_{m,p}(\mathbf{k}_0) \equiv u_{m,p}^*(\mathbf{k}_0) u_{-m,p}^*(-\mathbf{k}_0)$ and $\Lambda_{n,p}(\mathbf{k}_0) \equiv u_{n,p}^*(\mathbf{k}_0) u_{-n,p}^*(-\mathbf{k}_0)$ denote the form factors arising generally from projecting the interaction onto the band basis, and we introduced the shorthand notation $u_{-m,p}^*(-\mathbf{k}_0)$ to denote the coefficient associated with $c^\dagger(-\mathbf{k}_m)$ and $a_p^\dagger(-\mathbf{k}_0)$. The standard mean-field reduction for Eq. (15) leads to the gap equation $\Delta_{l,p} \equiv -U_0 \langle F_{l,p} \rangle$ for the pairing $\Delta_{l,p}$ in the BdG Hamiltonian in Eq. (4) for the superconducting state in the twisted double-layer, and $\Delta_{l,p}$ are obtained by minimizing \mathcal{F}_{SC} in Eq. (5).

Data availability

The data that support the findings presented in the main text and the Supplementary Information are available from the corresponding author upon reasonable request.

Code availability

The computer codes that support the findings presented in the main text and the Supplementary Information are available from the corresponding author upon reasonable request.

Received: 16 December 2022; Accepted: 2 March 2023;

Published online: 15 March 2023

References

1. Wilczek, F. Majorana returns. *Nat. Phys.* **5**, 614–618 (2009).
2. Alicea, J. New directions in the pursuit of Majorana fermions in solid state systems. *Rep. Prog. Phys.* **75**, 076501 (2012).
3. Beenakker, C. Search for Majorana Fermions in Superconductors. *Annu. Rev. Condens. Matter Phys.* **4**, 113 (2013).
4. Elliott, S. R. & Franz, M. Colloquium: Majorana fermions in nuclear, particle, and solid-state physics. *Rev. Mod. Phys.* **87**, 137 (2015).
5. Sarma, S. D., Freedman, M. & Nayak, C. Majorana zero modes and topological quantum computation. *npj Quantum Inf.* **1**, 1 (2015).
6. Read, N. & Green, D. Paired states of fermions in two dimensions with breaking of parity and time-reversal symmetries and the fractional quantum hall effect. *Phys. Rev. B* **61**, 10267 (2000).
7. Ivanov, D. A. Non-abelian statistics of half-quantum vortices in p -wave superconductors. *Phys. Rev. Lett.* **86**, 268 (2001).
8. Volovik, G. E. Fermion zero modes on vortices in chiral superconductors. *J. Exp. Theor. Phys. Lett.* **70**, 609–614 (1999).
9. Fu, L. & Kane, C. L. Superconducting proximity effect and majorana fermions at the surface of a topological insulator. *Phys. Rev. Lett.* **100**, 096407 (2008).
10. Sau, J. D., Lutchyn, R. M., Tewari, S. & Sarma, S. D. Generic new platform for topological quantum computation using semiconductor heterostructures. *Phys. Rev. Lett.* **104**, 040502 (2010).
11. Oreg, Y., Refael, G. & Von Oppen, F. Helical liquids and majorana bound states in quantum wires. *Phys. Rev. Lett.* **105**, 177002 (2010).
12. Alicea, J. Majorana fermions in a tunable semiconductor device. *Phys. Rev. B* **81**, 125318 (2010).
13. Mourik, V. et al. Signatures of majorana fermions in hybrid superconductor-semiconductor nanowire devices. *Science* **336**, 1003 (2012).
14. Qi, X.-L., Hughes, T. L. & Zhang, S.-C. Chiral topological superconductor from the quantum Hall state. *Phys. Rev. B* **82**, 184516 (2010).
15. He, Q.-L. et al. Chiral Majorana fermion modes in a quantum anomalous Hall insulator-superconductor structure. *Science* **357**, 6348 (2017).

16. Nadj-Perge, S. et al. Topological matter. Observation of Majorana fermions in ferromagnetic atomic chains on a superconductor. *Science* **346**, 6209 (2014).
17. Wang, D. et al. Evidence for Majorana bound states in an iron-based superconductor. *Science* **362**, 6412 (2018).
18. Liu, J., Potter, A. C., Law, K. T. & Lee, P. A. Zero-bias peaks in the tunneling conductance of spin-orbit-coupled superconducting wires with and without majorana end-states. *Phys. Rev. Lett.* **109**, 267002 (2012).
19. Zhang, H. et al. Quantized Majorana conductance. *Nature* **556**, 74–79 (2018).
20. Kayyalha, M. et al. Absence of evidence for chiral Majorana modes in quantum anomalous Hall-superconductor devices. *Science* **367**, 6473 (2020).
21. Bistritzer, R. & MacDonald, A. H. Moiré bands in twisted double-layer graphene. *Proc. Natl Acad. Sci. USA* **108**, 12233 (2011).
22. Cao, Y. et al. Correlated insulator behaviour at half-filling in magic-angle graphene superlattices. *Nature* **556**, 80–84 (2018).
23. Cao, Y. et al. Unconventional superconductivity in magic-angle graphene superlattices. *Nature* **556**, 43–50 (2018).
24. Wu, F., Lovorn, T., Tutuc, E., Martin, I. & MacDonald, A. H. Topological insulators in twisted transition metal dichalcogenide homobilayers. *Phys. Rev. Lett.* **122**, 086402 (2019).
25. Yankowitz, M. et al. Tuning superconductivity in twisted bilayer graphene. *Science* **363**, 1059 (2019).
26. Sharpe, A. L. et al. Emergent ferromagnetism near three-quarters filling in twisted bilayer graphene. *Science* **365**, 605–608 (2019).
27. Serlin, M. et al. Intrinsic quantized anomalous Hall effect in a moiré heterostructure. *Science* **367**, 900–903 (2020).
28. Nuckolls, K. P. et al. Strongly correlated Chern insulators in magic-angle twisted bilayer graphene. *Nature* **588**, 610–615 (2020).
29. Andrei, E. Y. et al. The marvels of moiré materials. *Nat. Rev. Mater.* **6**, 201–206 (2021).
30. Can, O. et al. High-temperature topological superconductivity in twisted double-layer copper oxides. *Nat. Phys.* **17**, 519–524 (2021).
31. Volkov, P. A., Wilson, J. H. & Pixley, J. H. Magic angles and current-induced topology in twisted nodal superconductors. Preprint at <https://arxiv.org/abs/2012.07860> (2012).
32. Zhao, S. Y. Frank et al. Emergent interfacial superconductivity between twisted cuprate superconductors. Preprint at <https://arxiv.org/abs/2108.13455> (2021).
33. Tummuru, T., Can, O. & Franz, M. Chiral p-wave superconductivity in a twisted array of proximitized quantum wires. *Phys. Rev. B* **103**, L100501 (2021).
34. Zhou, H., Xie, T., Taniguchi, T., Watanabe, K. & Young, A. F. Superconductivity in rhombohedral trilayer graphene. *Nature* **598**, 434–438 (2021).
35. Zhou, H. et al. Isospin magnetism and spin-polarized superconductivity in Bernal bilayer graphene. *Science* **375**, 6582 (2022).
36. Chou, Y.-Z., Wu, F., Sau, J. D. & Sarma, S. D. Acoustic-phonon-mediated superconductivity in rhombohedral trilayer graphene. *Phys. Rev. Lett.* **127**, 187001 (2021).
37. Chou, Y.-Z., Wu, F., Sau, J. D. & Sarma, S. D. Acoustic-phonon-mediated superconductivity in Bernal bilayer graphene. *Phys. Rev. B* **105**, L100503 (2022).
38. Crépel, V. & Fu, L. Spin-triplet superconductivity from excitonic effect in doped insulators. *Proc. Natl Acad. Sci. USA* **119**, e2117735119 (2022).
39. Kasahara, Y. et al. Enhancement of pairing interaction and magnetic fluctuations toward a band insulator in an electron-doped Li_xZrNCl superconductor. *Phys. Rev. Lett.* **103**, 077004 (2009).
40. Altland, A. & Zirnbauer, M. R. Nonstandard symmetry classes in mesoscopic normal-superconducting hybrid structures. *Phys. Rev. B* **55**, 1142 (1997).
41. Fujita, M., Wakabayashi, K., Nakada, K. & Kusakabe, K. Peculiar Localized State at Zigzag Graphite Edge. *J. Phys. Soc. Jpn.* **65**, 1920–1923 (1996).
42. Delplace, P., Ullmo, D. & Montambaux, G. Zak phase and the existence of edge states in graphene. *Phys. Rev. B* **84**, 195452 (2011).
43. Zhou, B. T., Yuan, N. F. Q., Jiang, H.-L. & Law, K. T. Ising superconductivity and Majorana fermions in transition-metal dichalcogenides. *Phys. Rev. B* **93**, 180501(R) (2016).
44. Mele, E. J. Commensuration and interlayer coherence in twisted bilayer graphene. *Phys. Rev. B* **81**, 161405(R) (2010).
45. Moon, P., Koshino, M. & Son, Y. Quasicrystalline electronic states in 30° rotated twisted bilayer graphene. *Phys. Rev. B* **99**, 165430 (2019).
46. Zhou, B. T., Egan, S. & Franz, M. Moiré flat Chern bands and correlated quantum anomalous Hall states generated by spin-orbit couplings in twisted homobilayer MoS_2 . *Phys. Rev. Res.* **4**, L012032 (2022).
47. Yao, W. et al. Quasicrystalline 30° twisted bilayer graphene as an incommensurate superlattice with strong interlayer coupling. *Proc. Natl Acad. Sci. USA* **115**, 6928–6933 (2018).
48. Pezzini, S. et al. 30° -twisted bilayer graphene quasicrystals from chemical vapor deposition. *Nano Lett.* **20**, 3313–3319 (2020).
49. Goerbig, M. & Montambaux, G. In *Dirac Matter* (eds Duplantier, B., Rivasseau, V. & Fuchs, J.-N.) 25–53 (Springer International Publishing, 2017).
50. Schnyder, A. P., Ryu, S., Furusaki, A. & Ludwig, A. W. W. Classification of topological insulators and superconductors in three spatial dimensions. *Phys. Rev. B* **78**, 195125 (2008).
51. Chiu, C.-K., Teo, J. C. Y., Schnyder, A. P. & Ryu, S. Classification of topological quantum matter with symmetries. *Rev. Mod. Phys.* **88**, 035005 (2016).
52. Sato, M., Tanaka, Y., Yada, K. & Yokoyama, T. Topology of Andreev bound states with flat dispersion. *Phys. Rev. B* **83**, 224511 (2011).
53. Schnyder, A. P. & Ryu, S. Topological phases and surface flat bands in superconductors without inversion symmetry. *Phys. Rev. B* **84**, 060504(R) (2011).
54. Chiu, C.-Kai & Schnyder, A. P. Classification of reflection-symmetry-protected topological semimetals and nodal superconductors. *Phys. Rev. B* **90**, 205136 (2014).
55. He, W.-Y. et al. Magnetic field driven nodal topological superconductivity in monolayer transition metal dichalcogenides. *Commun. Phys.* **1**, 40 (2018).
56. Heid, R. & Bohnen, K.-P. Ab initio lattice dynamics and electron-phonon coupling in Li_xZrNCl . *Phys. Rev. B* **72**, 134527 (2005).
57. Yin, Z. P., Kutepov, A. & Kotliar, G. Correlation-enhanced electron-phonon coupling: applications of gw and screened hybrid functional to bismuthates, chloronitrides, and other high- T_c superconductors. *Phys. Rev. X* **3**, 021011 (2013).
58. Tou, H., Maniwa, Y., Koiwasaki, T. & Yamanaka, S. Evidence for quasi-two-dimensional superconductivity in electron-doped $\text{Li}_{0.48}(\text{THF})_x\text{H}_y\text{NCl}$. *Phys. Rev. B* **63**, 020508(R) (2000).
59. Tou, H. et al. Upper critical field in the electron-doped layered superconductor $\text{ZrNCl}_{0.7}$: Magnetoresistance studies. *Phys. Rev. B* **72**, 020501(R) (2005).
60. Nakagawa, Y. et al. Gate-controlled BCS-BEC crossover in a two-dimensional superconductor. *Science* **372**, 6538 (2021).
61. Vakaryuk, V. & Leggett, A. J. Spin polarization of half-quantum vortex in systems with equal spin pairing. *Phys. Rev. Lett.* **103**, 057003 (2009).
62. Yip, S. K. & Sauls, J. A. Circular dichroism and birefringence in unconventional superconductors. *J. Low. Temp. Phys.* **86**, 257–290 (1992).
63. Can, O., Zhang, X.-X., Kallin, C. & Franz, M. Probing time reversal symmetry breaking topological superconductivity in twisted double layer copper oxides with polar Kerr effect. *Phys. Rev. Lett.* **127**, 157001 (2021).
64. Fischer, O., Kugler, M., Maggio-Aprile, I., Berthod, C. & Renner, C. Scanning tunneling spectroscopy of hightemperature superconductors. *Rev. Mod. Phys.* **79**, 353 (2007).
65. Liu, Y.-B., Zhang, Y., Chen, W.-Q. & Yang, F. High-angular-momentum topological superconductivities in twisted bilayer quasicrystal systems. *Phys. Rev. B* **107**, 014501 (2023).
66. Szabó, AndrásL. & Roy, B. Metals, fractional metals, and superconductivity in rhombohedral trilayer graphene. *Phys. Rev. B* **105**, L081407 (2022).
67. Chatterjee, S., Wang, T., Berg, E. & Zaletel, M. P. Inter-valley coherent order and isospin fluctuation mediated superconductivity in rhombohedral trilayer graphene. *Nat. Commun.* **13**, 6013 (2022).
68. Ghazaryan, A., Holder, T., Serbyn, M. & Berg, E. Unconventional superconductivity in systems with annular fermi surfaces: application to rhombohedral trilayer graphene. *Phys. Rev. Lett.* **127**, 247001 (2021).
69. Dong, Z. & Levitov, L. Superconductivity in the vicinity of an isospin-polarized state in a cubic Dirac band. Preprint at <https://arxiv.org/abs/2109.01133>.

Acknowledgements

The authors thank Oguzhan Can, Rafael Haenel, Christine Au-Yeung, Andrea Damasceli, Andreas Schnyder for illuminating discussions and communications. This work was supported by NSERC and the Canada First Research Excellence Fund, Quantum Materials and Future Technologies Program. B.T.Z. acknowledges the support of the Croucher Foundation.

Author contributions

B.T.Z. and M.F. conceived the idea. B.T.Z. developed the generalized DMSTB model and performed the major part of the calculations on the normal-state fermiology and superconducting phase diagram. S.E. and D.K. contributed to the edge state and vortex state calculations. B.T.Z. wrote the manuscript with contributions from all authors; M.F. supervised the project.

Competing interests

The authors declare no competing interests.

Additional information

Supplementary information The online version contains supplementary material available at <https://doi.org/10.1038/s42005-023-01165-5>.

Correspondence and requests for materials should be addressed to Benjamin T. Zhou or Marcel Franz.

Peer review information *Communications Physics* thanks the anonymous reviewers for their contribution to the peer review of this work. Peer reviewer reports are available.

Reprints and permission information is available at <http://www.nature.com/reprints>

Publisher's note Springer Nature remains neutral with regard to jurisdictional claims in published maps and institutional affiliations.



Open Access This article is licensed under a Creative Commons Attribution 4.0 International License, which permits use, sharing, adaptation, distribution and reproduction in any medium or format, as long as you give appropriate credit to the original author(s) and the source, provide a link to the Creative Commons license, and indicate if changes were made. The images or other third party material in this article are included in the article's Creative Commons license, unless indicated otherwise in a credit line to the material. If material is not included in the article's Creative Commons license and your intended use is not permitted by statutory regulation or exceeds the permitted use, you will need to obtain permission directly from the copyright holder. To view a copy of this license, visit <http://creativecommons.org/licenses/by/4.0/>.

© The Author(s) 2023